Plastic strain rate quantified from dislocation dynamics in dusty plasma shear flows

Shaoyu Lu, Dong Huang, and Yan Feng*

Center for Soft Condensed Matter Physics and Interdisciplinary Research, College of Physical Science and Technology, Soochow University, Suzhou 215006, China

(Received 20 April 2021; accepted 29 May 2021; published 24 June 2021)

Dynamics of dislocations and defects are investigated in 2D dusty plasma experiments with two counterpropagating flows. It is experimentally demonstrated that the Orowan equation is able to accurately determine the plastic strain rate from the motion of dislocations, well agreeing with the shear rate defined from the drift velocity gradient. For a higher shear rate, the studied system is in the liquidlike flow state, as a result, the determined shear rate from the Orowan equation deviates from its definition. The obtained probability distribution function of dislocations from the experiments clearly shows that the dislocation motion can be divided into the local and gliding ones. All findings above are further verified by the corresponding Langevin dynamical simulations with various levels of shear rates. The dislocation and defect analysis results from these simulations clearly indicate that the defect and dislocation dynamics in the sheared dusty plasmas clearly exhibit two stages as the shear rate increases.

DOI: 10.1103/PhysRevE.103.063214

I. INTRODUCTION

In the investigations of the crystal plasticity [1], the dislocation dynamics are often used to predict the macroscopic mechanical properties of materials [1]. For example, Orowan originally interpreted the mechanism of the plastic flow as the dynamical process of the dislocation motion using an analytical expression, known as the Orowan equation [2]. The Orowan equation is defined as

$$\dot{\gamma} = \rho \vec{b} \cdot \vec{v}, \tag{1}$$

where $\dot{\gamma}$ is the plastic strain rate, while ρ, $\vec{b}$, and $\vec{v}$ are the density, the Burgers vector [3], and the average velocity of dislocations, respectively. The Orowan equation, or its modified form, is widely used to determine the plastic strain rate for various solid materials [4–11]. However, in these studies [4–11], the dislocation velocity is obtained from either the empirical equations or the numerical simulations. From our literature search, we have not found the use of the Orowan equation with the direct experimental measurements of dislocations or defects.

To measure the dislocation velocity accurately in experiments, two-dimensional (2D) physical systems are desired, due to the precise measurements of positions and velocities [12]. The typical 2D physical systems include electrons on a liquid helium surface [13], ions confined magnetically in a Penning trap [14], granular materials [15], colloids [16], and dusty plasmas [12]. All of these 2D systems [12–16] provide the direct experimental observations of individual "particles," so that the corresponding dislocations or defects can be easily identified.

Dusty plasma, or complex plasma, typically refers to a partially ionized gas containing micron-sized dust particles [17–28]. In the typical laboratory conditions, these dust particles are highly charged to $-10^3 \sim -10^5 e$, so that they can be confined and levitated in the plasma sheath, forming a single-layer suspension, i.e., 2D dusty plasma [12,29]. Due to their high charge, these dust particles are strong coupled, exhibiting collective behaviors of either liquids [22,27,30–34] or solids [35–42]. The experiment diagnostic of direct video imaging in 2D dusty plasmas allows the individual particle tracking at the kinetic level [12,24]. Thus, from the static snapshots of 2D dust plasmas in experiments, the defects, including their locations, can be directly determined from the corresponding Voronoi diagrams [12,43,44], and then the dynamics of defects can be further investigated quantitatively, as we will study here.

The plastic deformation and the dislocation dynamics are both investigated in dusty plasma experiments. The plastic deformation under the slow uniaxial compression [39] shows that the lattice becomes locally sheared and this local strain is relaxed by shear slips. In Ref. [40], the slow plastic creep under shear is applied on 2D dusty plasmas, so that the exponents of the shear rate dependence on the shear stress and defect density are both determined. In Refs. [41,42], the experiment observations show that the dislocations may move in the glide plane faster than the transverse wave, even faster than the longitudinal wave. However, we have not found any investigations of the relation between the plastic deformation and the dislocation dynamics in dusty plasma experiments. Here, we would like to demonstrate the accuracy of the Orowan equation in 2D dusty plasma experiments, i.e., using the dislocation motion to quantitatively describe the plastic deformation.

This paper is organized as follows. In Sec. II, we briefly introduce the dusty plasma experiments containing shear flows, as well as the corresponding simulations. In Sec III, we calculate the shear rate using the Orowan equation, and compare

*fengyan@suda.edu.cn

it with the shear rate definition of the flow velocity gradient. Furthermore, we also calculate the probability distribution function (PDF) of the dislocation displacement, and study the dislocation dynamics as the shear rate increases. Finally, it is a brief summary.

II. SHEAR FLOW EXPERIMENTS AND SIMULATIONS

To demonstrate the accuracy of the Orowan equation, we use the data from two dusty plasma experiments [45,46] with different shear modulation methods. For these two experiments, micron-sized dust particles are introduced into RF plasma, forming a single layer suspension in a 2D triangular lattice [45,46]. Then, two laser beams are applied on the dusty plasma suspension to generate shear flows in the steady state. During the experiment, the motion of several thousand dust particles inside the field of view of the camera is recorded at the rate of 55 frame/s, with a resolution of 0.039 mm/pixel in Ref. [45] or 0.036 mm/pixel in Ref. [46]. The details of the experimental operations are presented in Refs. [45,46]. Next, we briefly summarize the difference between these two experiments, as well as the relevant parameters in our analysis.

In Experiment I [45], each laser beam is rastered in both the x and y directions in the Lissajous pattern inside a rectangle. As a result, all particles inside the two rectangles (about 4 mm width each in the y direction), are pushed in the $\pm\mathbf{x}$ directions by two laser beams, as shown in Fig. 1 of Ref. [45]. Then, a movie of the steady state shear flow containing 5000 frames is recorded for our data anlysis here. In this experiment [45], the Wigner-Seitz radius is $a = 0.26\,\mathrm{mm}$, the nominal 2D dusty plasma frequency is $\omega_{\mathrm{pd}} = 75\,\mathrm{s}^{-1}$, the screening parameter is $\kappa = a/\lambda_D = 0.5$, where λ_D is the screening length of the Yukawa potential, and the gas damping rate is $\nu_{\mathrm{gas}} = 2.7\,\mathrm{s}^{-1}$.

In Experiment II [46], two laser beams are rastered oppositely only in the $\pm\mathbf{x}$ directions, which are separated by 4.7 mm on the suspension. The full width at half maximum of the intensity profile of each manipulation laser beam is about 0.2 mm, which is about the Wigner-Seitz radius, narrow enough to manipulate one single particle in one moment. As a result, two narrow particle flows are generated by the laser manipulation, causing the shear-induced melting in the central region, and later 400 frames of the steady state shear flow are recorded for the data analysis here. In this experiment [46], the Wigner-Seitz radius is $a = 0.21\,\mathrm{mm}$, the nominal 2D dusty plasma frequency is $\omega_{\mathrm{pd}} = 86\,\mathrm{s}^{-1}$, the screening parameter is $\kappa = 0.47$, and the gas damping rate is $\nu_{\mathrm{gas}} = 2.7\,\mathrm{s}^{-1}$.

We calculate the flow velocity profile $\overline{V_x}$ of the steady state shear flow in these two experiments, as presented in the insets of Fig. 1. Here, we mainly focus on the central region of the profile, as marked between two vertical dashed lines in the two insets. For each of these two experiments, the flow velocity profile in the central region is always nearly linear, as the corresponding fit of the solid line shown in Fig. 1. The slope of the linear fit $\dot{\gamma} = \partial\overline{V_x}/\partial y$ is just the shear rate in the central region, which is $\dot{\gamma} = 0.00150\omega_{\mathrm{pd}}$ in Fig. 1(a) for Experiment I, and $\dot{\gamma} = 0.00906\omega_{\mathrm{pd}}$ in Fig. 1(b) for Experiment II, respectively. In Fig. 1, the flow velocity $\overline{V_x}$ at the center point slightly deviates from zero for both of the experiments, due to some nonideal features of the experiments, for example, the slight overall drift of all particles in the field of view. Note, Fig. 1(a)

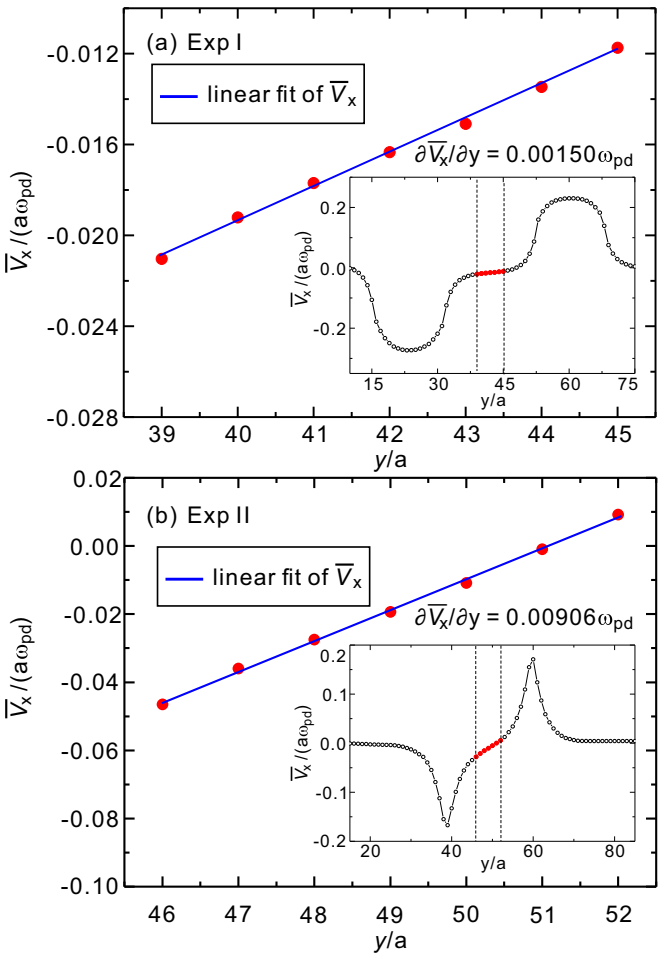

FIG. 1. Profiles of the flow velocity in the two two-dimensional (2D) dusty plasma experiments of Ref. [45] (a) and Ref. [46] (b), labeled as Exp I and Exp II, respectively, with different laser manipulation methods. For each of these two experiments, we mainly present the flow velocity profiles only in the central region, as the portion marked between two vertical dashed lines in the inset. Clearly, for each experiment, the flow velocity profile in the central region is always nearly linear, and the linear fit just corresponds to the shear rate, as the solid lines shown here. Note that, in our data analysis later, we always choose this central region as our studied region.

for Experiment I presents the linear fit of the flow velocity for the total recorded 5000 frames in the steady shear flow in Ref. [45], while in the later data analysis, this movie is divided into 5 parts, i.e., 1000 frames each, so that we can perform five measurements of the studied physical quantities to determine their uncertainty error bars. However, for Experiment II in Fig. 1(b), there are only 400 frames data in the steady shear flow, just enough to perform one measurement.

To mimic these two dusty plasma experiments [45,46], we also perform two types of simulations. We use Langevin dynamical simulations, with the equation of motion for each dust particle i

$$m\ddot{\mathbf{r}}_i = -\nabla\Sigma\phi_{ij} - \nu m\dot{\mathbf{r}}_i + \zeta_i(t) + \mathbf{F}_{\mathrm{ex}}. \tag{2}$$

Here, the four terms on the right-hand side of Eq. (2) are the particle-particle interaction, the frictional gas drag, the

Langevin random kicks, and the external manipulation force, respectively. The interparticle interaction is the Yukawa potential [47], $\phi(r) = Q^2\exp(-r/\lambda_D)/4\pi\epsilon_0 r$, where, Q is the particle charge and r is the distance between two particles. All simulations here are performed using LAMMPS [48].

The difference between these two dusty plasma experiments [45,46] is mainly in the laser manipulation method, where in Ref. [45] the laser beams are rastered nearly uniformly in a rectangular region, while in Ref. [46] the laser beams are rastered only in the x direction. Thus, for Simulation I, we specify this external force as $F_{ex} = \pm F_0\exp[-(y \pm 15)^8/10^8]ma\omega_{pd}^2$ in the x direction to achieve a pretty uniform rectangular region as in Experiment I [45]. While, for Simulation II, we specify this external force as $F_{ex} = \pm F_0\exp[-(y \pm 10)^2/0.25]ma\omega_{pd}^2$ in the x direction [49] to mimic the forces from the rastered laser beams in Experiment II [46]. As the verification of our specified expressions of F_{ex}, we confirm that, the obtained velocity profiles from these two types of simulations are very similar to the corresponding experimental results in Fig. 1. As compared with the experiments, our Langevin dynamical simulations also have some advantages. For example, the simulations contain much more data with a much longer time duration to provide more statistics, so that some nonideal features, like the nonzero flow velocity in the center, are greatly suppressed.

Here are some details in our Langevin dynamical simulations. The initial configuration of both types simulations starts from a perfect crystal in the solid state, containing $N = 4096$ particles. The initial value of the coupling parameters $\Gamma = Q^2/(4\pi\epsilon_0 a k_B T)$ is specified as 800 for all simulation runs, where T is the kinetic temperature of dust particles and k_B is the Boltzmann constant. We choose the screening parameter as $\kappa = 0.5$ and 0.47, and the gas damping rate as $\nu/\omega_{pd} = 0.036$ and 0.031, just corresponding to the conditions of Experiment I [45] and Experiment II [46], respectively. The integration time step is specified as $1.41 * 10^{-3}\omega_{pd}^{-1}$, and the time interval between two consecutive frames is $0.1414\omega_{pd}^{-1}$. The periodic boundary conditions are used in the both x and y directions. When the system generates the steady shear flow after the external force is applied, we record the positions and velocities of all particles in the temporal duration of $t\omega_{pd} = 14\,142$ for the later data analysis. Other simulation details are similar to Ref. [49].

III. RESULTS

A. Demonstration of the Orowan equation

For 2D systems, the expression of the Orowan equation [2] is expressed as $\dot{\gamma} = \frac{N_{dis}}{S} b\overline{v}_{dis}$, where ρ in Eq. (1) is replaced to N_{dis}/S, due to the two dimensionality. Here, S is the area of the analyzed region, N_{dis} is the dislocation number, and $\overline{v}_{dis}$ is the average velocity of dislocations in the analyzed region. The Burgers vector represents the magnitude and direction of the lattice distortion resulting from a dislocation in the crystal lattice [3]. For the Burgers vector of one dislocation in the triangular lattice, its magnitude is equal to one lattice constant, and its direction is parallel to the direction of the dislocation motion [50]. The dislocation and its location can be directly determined from the Voronoi diagram, calculated from particle positions in the 2D dusty plasma experiments. Then, we can obtain the static distribution of dislocations in each frame, and analyze the motion or dynamics of these dislocations by tracking them between consecutive frames. Thus, using the powerful diagnostic of the individual particle motion at the kinetic level in 2D dusty plasma experiments, we are able to determine the plastic strain rate directly from the corresponding Voronoi diagrams using the Orowan equation without any assumptions.

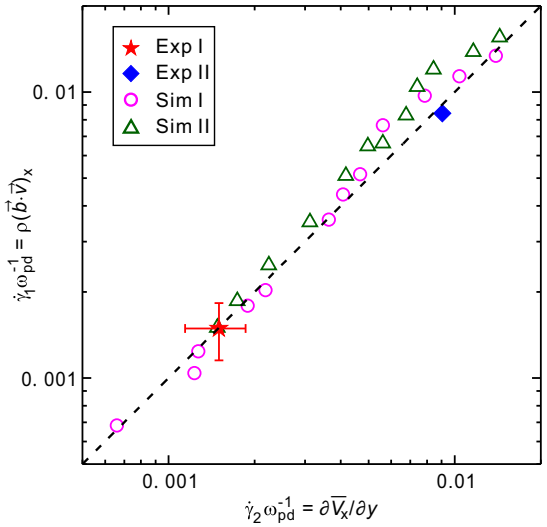

FIG. 2. Comparison of the shear rates obtained from various experiments and simulations using two different methods, one is from the Orowan equation $\dot{\gamma}_1 = \rho(\vec{b}\cdot\vec{v})_x$, the other is from the definition of the flow velocity gradient $\dot{\gamma}_2 = \partial\overline{V}_x/\partial y$. Clearly, when the shear rate is not very large, the shear rates obtained from these two methods well agree with each other, since all of our obtained data points almost fall on the straight dashed line of $\dot{\gamma}_1 = \dot{\gamma}_2$. Thus, using both 2D dusty plasma experiments and simulations, we demonstrate that the Orowan equation can accurately measure the macro plastic strain rate using the micro motion of dislocations, especially when $\dot{\gamma} \lesssim 0.005\omega_{pd}$.

As the major result of this paper, we demonstrate that the Orowan equation can accurately determine the shear rate in our 2D dusty plasma experiments. As presented in Fig. 2, we compare the shear rates calculated from the Orowan equation $\dot{\gamma}_1$ with those from the flow velocity gradient $\dot{\gamma}_2$, using the data from both our 2D dusty plasma experiments and the corresponding simulations. We find that all of our obtained data points almost fall on the straight dashed line of $\dot{\gamma}_1 = \dot{\gamma}_2$ in Fig. 2, especially when the shear rate is smaller than $0.005\omega_{pd}$. The results in Fig. 2 suggest that the shear rates obtained from these two methods are in good agreement with each other, especially when $\dot{\gamma} \lesssim 0.005\omega_{pd}$. Thus, the Orowan equation can be used to measure the macro plastic strain rate accurately from the micro motion of dislocations. Our numerical simulations further verify this demonstration. Note, in Fig. 2, the error bars of the data point of Experiment I come from the maximum and minimum of five measurements of the shear rates, while the data point of Experiment II is only obtained from one measurement, without an error bar.

When the shear rate is larger than $0.005\omega_{pd}$, our simulation results show that the shear rate calculated from the Orowan

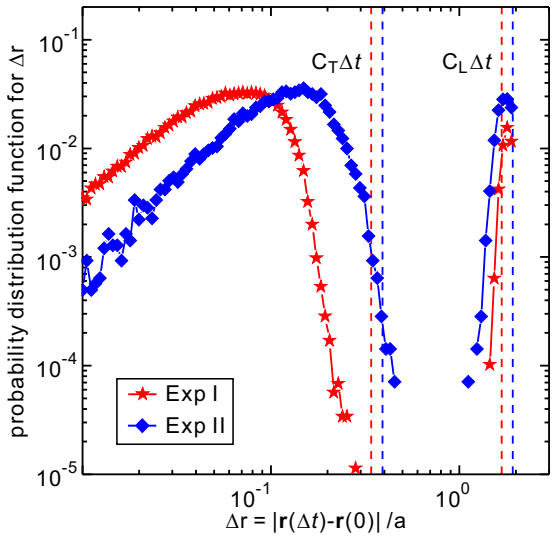

FIG. 3. Probability distributions function (PDF) of the dislocation displacement $\Delta r = |\mathbf{r}(\Delta t) - \mathbf{r}(0)|$ in the central analyzed region for the two different 2D dusty plasma experiments of Refs. [45,46]. For each experiment, there are two prominent peaks in the plot of the Δr distribution. We interpret that these two prominent peaks indicate that the dislocation motion contains two main modes during the plastic deformation, the local motion and the gliding motion [2]. Four vertical dashed lines indicate the displacement of $C_T\Delta t$ and $C_L\Delta t$ of the corresponding experiments. Here, C_L and C_T are the speeds of the longitudinal and transverse waves of 2D Yukawa crystals in the conditions of these two experiments.

equation $\dot{\gamma}_1$ seems to be slightly higher than those from the flow velocity gradient $\dot{\gamma}_2$. However, this deviation does not occur in the result of Experiment II. We speculate that the deviation between $\dot{\gamma}_1$ and $\dot{\gamma}_2$ in our simulations may be related to the state of the analyzed region, as we will discuss later. Note that, since the shear is applied only in the x direction, while using the Orowan equation, we only consider the components of the Burgers vector and the dislocation velocity in the x direction.

B. Dynamics of dislocations and defects

To further study the micro-mechanism of the plastic deformation in the sheared 2D dusty plasmas, we calculate the PDF of the dislocation displacement $\Delta r = |\mathbf{r}(\Delta t) - \mathbf{r}(0)|$ in the central analyzed regions, as shown in Fig. 3. For both of the experiments in Refs. [45,46], there are two prominent peaks in the distribution of Δr, as in Fig. 3. From our interpretation, these two prominent peaks represent two main modes of the dislocation motion during the plastic deformation, which are the local motion and the gliding motion [2]. Note, here Δr is calculated from the variation of the location of each dislocation between two consecutive frames, within the time interval Δt, which are $1.364\omega_{\rm pd}^{-1}$ and $1.564\omega_{\rm pd}^{-1}$ for Experiments I and II, respectively.

To compare the dislocation displacement Δr with the propagation distance of the longitudinal and transverse waves during the time interval Δt, we also add four vertical dashed lines of $C_T\Delta t$ and $C_L\Delta t$ in Fig. 3. Here C_L and C_T are the longitudinal and transverse wave speeds of 2D Yukawa solids with the same κ value in these two experiments. For Experiment I [45], the central analyzed region is in the solid state, as a result, all data points of Δr related to the first peak are always less than $C_T\Delta t$, i.e., the local motion of dislocations is always slower than transverse sound speed. However, in Experiment II [46], the analyzed region completely melts due to the shear flow, as a result, some data points of Δr related to the first peak do exceed $C_T\Delta t$. In addition, in Fig. 3, there is small probability that the gliding distance of the dislocation can exceed $C_L\Delta t$, which is the further experimental verification of the supersonic dislocations, as observed in the previous dusty plasma experiments of Refs. [41,42].

For the comparison with the experimental results, we also calculate the PDF of the dislocation displacement Δr using our simulations with various shear rates, as shown in Fig 4. For both types of our simulations, the PDF of the dislocation displacement also contains two prominent peaks, the same as the experimental results in Fig. 3. For various shear rates shown here, the most probability distribution of Δr, i.e., the peak location of the local motion, increases monotonically with the shear rate, while the location of the second peak remains almost unchanged. When the shear rate increases, the temperature of the analyzed region substantially increases due to the viscous heating effect [45], so that the thermal motion of dislocation is also enhanced, causing the peak location of the local motion increases. The second peak of Δr represents the gliding motion of dislocations, and the units of the gliding displacement should be proportional to the length of the Burgers vector, when a dislocation glides from one position to the other adjacent site. For the gliding motion of dislocations, the location of Δr related to the second peak seems to be always at the location of $\Delta r \approx 2a$ for both experiments and simulations, as shown in Figs. 3 and 4. This peak location just corresponds to the gliding displacement of the dislocation in one step, which is just one lattice constant of $b \approx 2a$ in the triangular lattice, i.e., the length of the Burgers vector [50]. Note, the value of $C_L\Delta t$ in Fig. 3 is much larger than $C_L\Delta t$ in Fig. 4, because Δt between two consecutive frames in our simulations is $0.1414\omega_{\rm pd}^{-1}$, only about one tenth of the experimental time interval in Fig. 3.

Figure 4 provides the detailed dynamics of the local and gliding motions of dislocations. For the dislocation local motion, some data points of Δr related to the first peak can exceed $C_T\Delta t$ when $\dot{\gamma} > 0.005\omega_{\rm pd}$, however, when $\dot{\gamma} < 0.005\omega_{\rm pd}$, all data points related to the first peak of Δr are entirely less than $C_T\Delta t$, as shown in Fig. 4. These features are similar to the experimental results in Fig. 3. In fact, for Experiment I and Experiment II, the analyzed regions are in the solid and liquid states, respectively. Here, we can divide the simulation data points into two groups of the solid and liquid states of the analyzed region, respectively, as indicated by the filled and open symbols in Fig. 4. For the filled symbols corresponding to the solid state of the central region, all data points corresponding to the first peak of Δr cannot exceed $C_T\Delta t$, not for the open symbols of the liquid state of the central region.

We also calculate the most probability distribution of Δr and the total probability of the dislocation gliding motion as in Figs. 5(a) and 5(b), so that the effect of the shear rate on the local and gliding motions can be quantified. As shown in

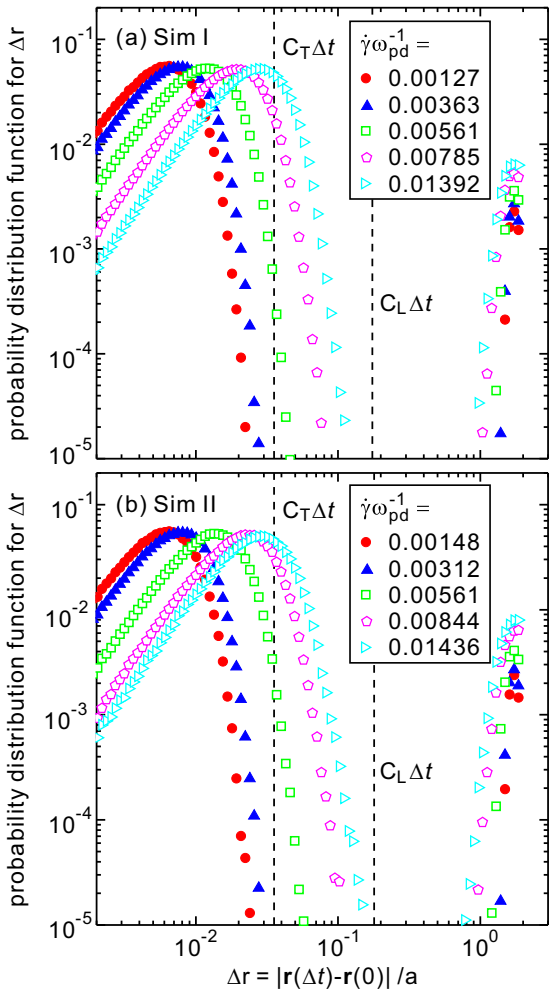

FIG. 4. Probability distribution function of the dislocation displacement Δr in the central region obtained from two types of 2D Yukawa simulations. The PDF of the dislocation displacement contains two prominent peaks corresponding to the local and gliding motions, consistent with our experimental results in Fig. 3. For both types of simulations, when the shear rate increases, the most probability distribution of Δr, i.e., the peak location of the local motion, increases monotonically, while the individual gliding displacement of dislocations nearly remains unchanged. The dynamics around the first peak of the dislocation displacement Δr are related to the thermal motion of the 2D Yukawa system. When the shear rate is higher, the viscous heating effect [45] substantially increases the temperature of the analyzed region, so that the location of the first peak increases. The gliding displacement of dislocations is unchanged for different shear rates, because the gliding displacement is proportional to the length of the Burgers vector, which is one lattice constant.

Figs. 5(a) and 5(b), it seems that the most probability distribution of Δr and the total probability of the dislocation gliding motion exhibit the same variation trend with the shear rate, which can be divided into two distinctive stages. In the first stage of $\dot{\gamma} \lesssim 0.005\omega_{pd}$, they both increase slowly, while in the second stage of $\dot{\gamma} > 0.005\omega_{pd}$, they both increase steeply, until their growth rates both slow down gradually when $\dot{\gamma} \gtrsim 0.008\omega_{pd}$.

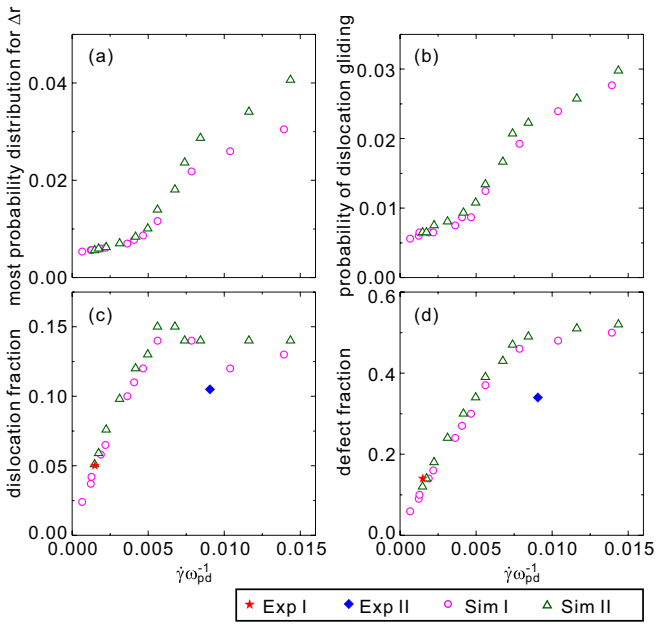

FIG. 5. The most probability distribution of the dislocation displacement (a), the total probability of the dislocation gliding motion (b), and the dislocation fraction (c), as well as the defect fraction (d) in the central analyzed regions, as the functions of the shear rate $\dot{\gamma}$. When $\dot{\gamma} \lesssim 0.005\omega_{pd}$, from panels (a) and (b), both the most probability distribution of the dislocation displacement and the total probability of the dislocation gliding motion increase slowly. Within this range of the shear rate, the dislocation fraction increases with the shear rate monotonically to its maximum when $\dot{\gamma} \approx 0.005\omega_{pd}$ in panel (c). When $\dot{\gamma} \approx 0.005\omega_{pd}$, the defect fraction from the Voronoi diagrams is ≈0.3 as shown in panel (d), corresponding to the typical liquid state as in Ref. [12]. In panel (d), when $\dot{\gamma} \approx 0.008\omega_{pd}$, the defect fraction reaches the saturation level, and the increase of the total probability of the dislocation gliding motion in panel (b) slows down gradually.

The fractions of the dislocation and defect for various shear rates are presented in Figs. 5(c) and 5(d). When $\dot{\gamma} \lesssim 0.005\omega_{pd}$, the dislocation fraction increases with the shear rate monotonically to its maximum, as in Fig. 5(c). Within this shear rate range, the increase of the most probability distribution of Δr and the total probability of the dislocation gliding motion are not substantial, as shown in Figs. 5(a) and 5(b). According to the definition of the Orowan equation, Eq. (1), the plastic strain rate is proportional to the product of the density and velocity of dislocations here. When $\dot{\gamma} \lesssim 0.005\omega_{pd}$, the increase of the dislocation velocity v is very small, since the steady particle flow has not been generated yet. As a result, the increase of the plastic strain rate $\dot{\gamma}$ should be mainly due to the increase of the dislocation density ρ from Eq. (1). As shown in Fig. 5(d), the defect fraction increases monotonically with the shear rate, until reaching its saturation level when $\dot{\gamma} \approx 0.008\omega_{pd}$, when the increase of the total probability of the dislocation gliding motion slows down.

When the shear rate increases from zero, the state of the central analyzed region changes from the solid to the liquid. Thus, we speculate that the different behaviors of the dislocation dynamics in the ranges of the larger and smaller shear rates mentioned above are related to the different states of the

analyzed region. As shown in Fig. 5(d), when $\dot{\gamma} \approx 0.005\omega_{\rm pd}$, the defect fraction from the Voronoi diagrams is around 0.3, corresponding to the typical liquid state as in Ref. [12]. When the shear rate is smaller than $0.005\omega_{\rm pd}$, the analyzed region is closer or almost in solid state, so that the shear flow in this region is the typical plastic flow, just the typical condition for the use of the Orowan equation. When the shear rate is larger than $0.005\omega_{\rm pd}$, the analyzed region is in the liquid state, so that the shear flow changes from the plastic flow to the liquidlike flow as in Ref. [51], which is not typical for the use of the Orowan equation any more. As a result, the use of the Orowan equation with the liquidlike flow systems may contains some errors, as the deviation between the shear rates determined from two methods in Fig. 2 for the higher shear rates $\gtrsim 0.005\omega_{\rm pd}$.

IV. SUMMARY

To summarize, in the 2D dusty plasma experiments containing shear flows, we demonstrate that the Orowan equation can be used to determine the shear rate. For both 2D dusty plasma experiments, we find that the plastic strain rate determined from the Orowan equation using the motion of dislocations well agrees with the shear rate defined from the drift velocity gradient. In our literature search, we have not found any previous experimental demonstration of the Orowan equation in any physical systems. All of these findings are verified by our Langevin dynamical simulations of the shear flows in dusty plasmas performed here, with 24 different levels of the shear rates. For higher shear rates, in our simulations, the studied system is in the liquidlike flow state, not typical for the use of the Orowan equation, as a result, the shear rate determined from the Orowan equation deviates from its definition.

In addition, to understand the microscopic mechanism of the plastic deformation and shear flow, we also study the detailed dislocation/defect dynamics for various shear rates in our experiments and simulations. We find that, as the shear rate increases, the defect/dislocation dynamics in the sheared dusty plasmas clearly exhibit the two-stage behavior. When the shear rate $\dot{\gamma}/\omega_{\rm pd} \lesssim 0.005$, the studied region is in the solid state, the local and gliding motions of dislocation are not effected by the shear rate much, the plastic strain rate here is mainly proportional to the dislocation density. When the shear rate $\dot{\gamma}/\omega_{\rm pd} \gtrsim 0.005$, the dislocation fraction is saturated, and the system is in the liquidlike flow state, where the most probability distribution of the dislocation displacement increases steeply with the shear rate.

ACKNOWLEDGMENTS

Work was supported by the National Natural Science Foundation of China under Grant No. 11875199, the 1000 Youth Talents Plan, startup funds from Soochow University, and the Priority Academic Program Development (PAPD) of Jiangsu Higher Education Institutions.

[1] P. Gillis and J. Gilman, J. Appl. Phys. **36**, 3370 (1965); **36**, 3380 (1965).
[2] E. Orowan, Proc. Phys. Soc. London **52**, 8 (1940).
[3] J. M. Burgers, Proc. Kon. Ned. Akad. Wetenschap **42**, 293 (1939); **42**, 378 (1939).
[4] M. Goerdeler and G. Gottstein, Mater. Sci. Eng. A **309**, 377 (2001).
[5] G. A. Malygin, S. L. Ogarkov, and A. V. Andriyash, Phys. Solid State **55**, 780 (2013).
[6] P. Fernandez-Zelaia, B. S. Adair, V. M. Barker, and S. D. Antolovich, Metall. Mater. Trans. A **46**, 5596 (2015).
[7] F. Boioli, P. Carrez, P. Cordier, B. Devincre, and M. Marquille, Phys. Rev. B **92**, 014115 (2015).
[8] W. Chen, T. Kitamura, and M. Feng, Mater. Sci. Eng. A **726**, 137 (2018).
[9] G. Ananthakrishna and S. K, Phys. Rev. B **97**, 104103 (2018).
[10] S. Saimoto, Acta Mater. **174**, 43 (2019).
[11] J. Lee and H. Jeong, Metals **9**, 500 (2019).
[12] Y. Feng, J. Goree, and B. Liu, Phys. Rev. Lett. **100**, 205007 (2008).
[13] C. C. Grimes and G. Adams, Phys. Rev. Lett. **42**, 795 (1979).
[14] T. B. Mitchell, J. Bollinger, X. Huang, and W. M. Itano, and D. H. E. Dubin., Phys. Plasmas **6**, 1751 (1999).
[15] P. M. Reis, R. A. Ingale, and M. D. Shattuck, Phys. Rev. Lett. **96**, 258001 (2006).
[16] C. Eisenmann, U. Gasser, P. Keim, G. Maret, and H. H. von Grunberg, Phys. Rev. Lett. **95**, 185502 (2005).
[17] H. M. Thomas and G. E. Morfill, Nature (London) **379**, 806 (1996).
[18] L. I, W. Juan, C. Chiang, and J. Chu, Science **272**, 1626 (1996).
[19] A. Melzer, A. Homann, and A. Piel, Phys. Rev. E **53**, 2757 (1996).
[20] M. S. Murillo, Phys. Rev. Lett. **85**, 2514 (2000).
[21] R. L. Merlino and J. A. Goree, Phys. Today **57**, 32 (2004).
[22] G. J. Kalman, P. Hartmann, Z. Donkó, and M. Rosenberg, Phys. Rev. Lett. **92**, 065001 (2004).
[23] V. E. Fortov, A. V. Ivlev, S. A. Khrapak, A. G. Khrapak, and G. E. Morfill, Phys. Rep. **421**, 1 (2005).
[24] G. E. Morfill and A. V. Ivlev, Rev. Mod. Phys. **81**, 1353 (2009).
[25] A. Piel, *Plasma Physics* (Springer, Heidelberg, 2010).
[26] M. Bonitz, C. Henning, and D. Block, Rep. Prog. Phys. **73**, 066501 (2010).
[27] A. Melzer, A. Schella, J. Schablinski, D. Block, and A. Piel, Phys. Rev. E **87**, 033107 (2013).
[28] E. Thomas, Jr., U. Konopka, R. L. Merlino, and M. Rosenberg, Phys. Plasmas **23**, 055701 (2016).
[29] K. Qiao, J. Kong, J. Carmona-Reyes, L. S. Matthews, and T. W. Hyde, Phys. Rev. E **90**, 033109 (2014).
[30] Z. Donkó, J. Goree, P. Hartmann, and K. Kutasi, Phys. Rev. Lett. **96**, 145003 (2006).
[31] C.-L. Chan and I. Lin, Phys. Rev. Lett. **98**, 105002 (2007).
[32] B. Liu and J. Goree, Phys. Rev. Lett. **100**, 055003 (2008).
[33] T. Ott and M. Bonitz, Phys. Rev. Lett. **103**, 195001 (2009).
[34] Y. Feng, J. Goree, and B. Liu, Phys. Rev. Lett. **105**, 025002 (2010).

[35] M. S. Murillo, Phys. Plasmas **11**, 2964 (2004).
[36] A. Melzer, A. Schella, J. Schablinski, D. Block, and A. Piel, Phys. Rev. Lett. **108**, 225001 (2012).
[37] P. Hartmann, A. Douglass, J. C. Reyes, L. S. Matthews, T. W. Hyde, A. Kovács, and Z. Donkó, Phys. Rev. Lett. **105**, 115004 (2010).
[38] E. Thomas, Jr., B. Lynch, U. Konopka, R. L. Merlino, and M. Rosenberg, Phys. Plasmas **22**, 030701 (2015).
[39] C. Durniak and D. Samsonov, Phys. Rev. Lett. **106**, 175001 (2011).
[40] P. Hartmann, A. Z. Kovács, A. M. Douglass, J. C. Reyes, L. S. Matthews, and T. W. Hyde, Phys. Rev. Lett. **113**, 025002 (2014).
[41] V. Nosenko, S. Zhdanov, and G. E. Morfill, Phys. Rev. Lett. **99**, 025002 (2007).
[42] V. Nosenko, G. E. Morfill, and P. Rosakis, Phys. Rev. Lett. **106**, 155002 (2011).
[43] R. A. Quinn and J. Goree, Phys. Rev. E **64**, 051404 (2001).
[44] V. Nosenko, S. K. Zhdanov, A. V. Ivlev, C. A. Knapek, and G. E. Morfill, Phys. Rev. Lett. **103**, 015001 (2009).
[45] Y. Feng, J. Goree, and B. Liu, Phys. Rev. Lett. **109**, 185002 (2012); Phys. Rev. E **86**, 056403 (2012).
[46] D. Huang, S. Lu, X. Shi, J. Goree, and Y. Feng (unpublished).
[47] U. Konopka, G. E. Morfill, and L. Ratke, Phys. Rev. Lett. **84**, 891 (2000).
[48] See http://lammps.sandia.gov.
[49] D. Huang, S. Lu, and Y. Feng, Phys. Rev. E **103**, 013211 (2021).
[50] D. R. Nelson and B. I. Halperin, Phys. Rev. B **19**, 2457 (1979).
[51] B. Liu and J. Goree, Phys. Plasmas **24**, 103702 (2017).